FISEVIER

Contents lists available at ScienceDirect

Applied Surface Science Advances

journal homepage: www.sciencedirect.com/journal/applied-surface-science-advances





Scale-dependent roughness parameters for topography analysis

Antoine Sanner ^{a,b}, Wolfram G. Nöhring ^a, Luke A. Thimons ^c, Tevis D.B. Jacobs ^c, Lars Pastewka ^{*,a,b}

- ^a Department of Microsystems Engineering, University of Freiburg, Georges-Köhler-Allee 103, Freiburg 79110, Germany
- ^b Cluster of Excellence livMatS, Freiburg Center for Interactive Materials and Bioinspired Technologies, University of Freiburg, Georges-Köhler-Allee 105, Freiburg 79110, Germany
- c Department of Mechanical Engineering and Materials Science, University of Pittsburgh, 3700 O'Hara Street, Pittsburgh, Pennsylvania 15261, USA

ARTICLE INFO

Keywords: Surface roughness Autocorrelation function Spectral analysis Variable bandwidth method Tip convolution artifacts

ABSTRACT

The failure of roughness parameters to predict surface properties stems from their inherent scale-dependence; in other words, the measured value depends on how the parameter was measured. Here we take advantage of this scale-dependence to develop a new framework for characterizing rough surfaces: the Scale-Dependent Roughness Parameters (SDRP) analysis, which yields slope, curvature, and higher-order derivatives of surface topography at many scales, even for a single topography measurement. We demonstrate the relationship between SDRP and other common statistical methods for analyzing surfaces: the height-difference autocorrelation function (ACF), variable bandwidth methods (VBMs) and the power spectral density (PSD). We use computer-generated and measured topographies to demonstrate the benefits of SDRP analysis, including: novel metrics for characterizing surfaces across scales, and the detection of measurement artifacts. The SDRP is a generalized framework for scale-dependent analysis of surface topography that yields metrics that are intuitively understandable.

1. Introduction

Surface roughness is primarily characterized in terms of scalar parameters; especially common are the root-mean-square (rms) height and slope, which are the rms deviations from the mean height and mean slope. Some variant of these quantities is computed by all surface topography instruments, and they are often reported to describe surface topography in publications. These quantities are useful for describing the amplitude of spatial fluctuations in height and slope across the measured topography. However, a core issue with these roughness parameters is that all of them explicitly depend on the scale of the measurement [1]: The rms height depends on the lateral size (largest scale) of the measurement; the rms slope depends on the resolution (smallest scale) of the measurement. A direct demonstration of this effect on real-world measurements can be found in Refs. [2,3]. We note that some standardized expressions for obtaining these values, such as Rq from ISO 4287 [4] include high- and low-frequency filtering. These values are still strongly scale-dependent, but now the relevant scale is the size of the filter rather than the size of the measurement.

The scale dependence of these values is typically a signature of the multi-scale nature of surface topography. A simple illustration is given in

a classic article by Benoit Mandelbrot on the length of coastlines [5]. Mandelbrot illustrated, that the length L_{coast} of a coastline depends on the length of the yard stick ℓ used to measure it. A smaller yard stick picks up finer details and hence leads to longer coastlines. For (self-affine) fractals [6], the functional relationship $L_{\text{coast}}(\ell)$ is a power-law whose exponent characterizes the fractal dimension of the coastline. In the case of a surface topography measurement, ℓ corresponds to the resolution of the scientific instrument used to measure the topography and the property corresponding to the length of a coastline is the true surface area $S(\ell)$ of the topography. We have in prior work directly demonstrated that $S(\ell)$ (and also the rms slope and curvature) scales with measurement resolution ℓ [2,3,7]. This scaling of the surface area has, for example, direct relevance to adhesion between soft surfaces [7]. Many surfaces do not behave as ideal fractals, but nearly all surfaces exhibit some form of size dependence of the roughness parameters discussed above. This is because processes that shape surfaces, such as fracture [8-10], plasticity [11-14] or erosion [15], all lead to multi-scale, fractal-like topography over a range of length scales.

Here, we suggest a route to generalize these (and other) geometric properties of measured topography to explicitly contain a notion of measurement scale. We define the individual roughness parameter as a

E-mail address: lars.pastewka@imtek.uni-freiburg.de (L. Pastewka).

^{*} Corresponding author.

function of scale ℓ over which it is measured, leading to curves identifying the value of the parameter as a function of ℓ . Unlike above, where ℓ was restricted to the resolution of the instrument or some fixed filter cutoff, we now broaden the concept of this scale ℓ to refer to any size over which a parameter is computed. For a given topography scan, it can range from the pixel size up to the scan size. We term the resulting curves the scale-dependent roughness parameters (SDRPs) and outline the relationship to three common characterization techniques: the heightdifference autocorrelation function (ACF), the variable bandwidth method (VBM) and the power spectral density (PSD). SDRPs are useful because they are easily interpreted: While it is difficult to attach a geometric meaning to a certain value of the PSD (where even units can be unclear [1]), the slope and curvature both have simple geometric interpretations. Since slope and curvature are also the primary ingredients for modern theories of contact between rough surfaces [16-24], SDRPs are directly connected to functional properties of rough surfaces. Finally, we illustrate below how SDRPs can be used to estimate tip-radius artifacts in contact-based measurements, such as scanning probe microscopy and stylus profilometry.

2. Analysis methodology

2.1. Computing typical roughness parameters in real space

Surface topography is commonly described by a function h(x, y), where x and y are the coordinates in the plane of the surface. This is sometimes called the Monge representation of a surface, which is an approximation as it excludes overhangs (reentrant surfaces). A real measurement does not yield a continuous function but height values

$$h_{kl} = h(x_k, y_l) \tag{1}$$

on a set of discrete points x_k and y_l . Measurements are often taken on equidistant samples where $x_k = k\Delta x$ and $y_l = l\Delta y$, where Δx and Δy are the distance between the sample-points in their respective directions. Furthermore $k \in [0, N_x - 1]$ and $l \in [0, N_y - 1]$ where $N_x \times N_y$ is the total number of sample points.

Topographies are often random such that h_{kl} is a random process and its properties must be described in a statistical manner. Starting with Longuet-Higgins [25,26] and Nayak [27], many authors have discussed this random process model of surface roughness, yet the most commonly used roughness parameters have remained simple.

We will illustrate the following concepts using the one-dimensional case, i.e. for line scans or profiles. In many real scenarios, even areal topographic measurements are interpreted as a series of line scans. This is for example the case in atomic force microscopy (AFM), where a topographic map is stitched together from a series of adjacent line scans. Because of temporal (instrumental) drift, these line scans may not be perfectly aligned and the "scan"-direction is then the preferred direction for statistical evaluation. In the following mathematical development, we will implicitly assume that all values are obtained by averaging over these consecutive scans, but we will not write this average explicitly in the equations that follow. Extension to true two-dimensional topography maps of the ideas presented here is straightforward and briefly discussed in Appendix A.

The most straightforward statistical property is the root-mean-square (rms) height,

$$h_{\text{rms}} = \left\langle h_k^2 \right\rangle^{1/2} \equiv \left\langle h^2(x) \right\rangle^{1/2},\tag{2}$$

where the average $\langle \cdot \rangle$ is taken over all indices k. (We will omit the explicit index k in the following equations.) The rms height measures the amplitude of height fluctuations on the topography, where the midline is defined as h=0. In addition to the height fluctuation, we can also quantify the amplitude of slopes,

$$h'_{\text{rms}} = \left\langle \left(\frac{D}{Dx}h(x)\right)^2 \right\rangle^{1/2},\tag{3}$$

where D/Dx is a discrete derivative in the *x*-direction.

A common way to compute discrete derivatives on experimental data is to use a *finite-differences* approximation. Finite-differences approximate the height h(x) locally as a polynomial (a Taylor series expansion). The first derivative can then be computed as

$$\frac{\partial}{\partial x}h(x) \approx \frac{D}{Dx}h(x) = \frac{h(x + \Delta x) - h(x)}{\Delta x}.$$
 (4)

This expression is called the first-order right-differences scheme. We will use the symbol D for the discrete derivatives, and the term "order" here refers to the truncation order, or how fast the error decays with grid spacing Δx : it drops linearly with decreasing Δx in this scheme. Another interpretation is that the truncation order gives the highest exponent of the polynomial used to interpolate between the points x and $x + \Delta x$. The derivative of a linear interpolation is constant between these points and given by Eq. (4).

We can also quantify the amplitude of higher derivatives,

$$h_{\rm rms}^{(\alpha)} = \left\langle \left(\frac{D^{\alpha}}{Dx^{\alpha}}h(x)\right)^{2}\right\rangle^{1/2},\tag{5}$$

where $\alpha=2$ yields the rms curvature. A discrete formulation of the second derivative is

$$\frac{D^2}{Dx^2}h(x) = \frac{h(x + \Delta x) - 2h(x) + h(x - \Delta x)}{\Delta x^2}.$$
 (6)

This expression is called the second-order central-differences approximation. Again, this can be interpreted as fitting a second-order polynomial to the three points $x - \Delta x$, x, and $x + \Delta x$, and interpreting the (constant) second derivative of this polynomial as the approximate second derivative of the discrete set of data points. The third derivative is given by

$$\frac{D^{3}}{Dx^{3}}h(x) = \frac{h(x+2\Delta x) - 3h(x+\Delta x) + 3h(x) - h(x-\Delta x)}{\Delta x^{3}},$$
(7)

which again can be interpreted in terms of fitting a cubic polynomial to (four) collocation points.

We can generally write the discrete derivative as a weighted sum over the collocation points x_k ,

$$\frac{D^{\alpha}}{Dx^{\alpha}}h(x_k) = \frac{1}{\Delta x^{\alpha}} \sum_{l=-\infty}^{\infty} c_l^{(\alpha)}h(x_{k+l}). \tag{8}$$

The values $c_l^{(\alpha)}$ are called the *stencil* of the derivative operator and α indicates the order of the derivative. For the above derivatives,

$$c_0^{(1)} = -1, c_1^{(1)} = 1, (9)$$

$$c_0^{(2)} = -2, c_{+1}^{(2)} = 1$$
 and (10)

$$c_0^{(3)} = 3, c_1^{(3)} = -3, c_{-1}^{(3)} = -1, c_2^{(3)} = 1,$$
 (11)

and all other $c_l^{(\alpha)}$ s are zero. Higher-order derivatives lead to wider stencils.

2.2. Computing scale-dependent roughness parameters in real space

The discrete derivatives of the preceding section are all defined on the smallest possible scale that is given by the sample spacing Δx and have an overall width of $\alpha \Delta x$. It is straightforward to attach an explicit scale to these derivatives, by evaluating Eq. (8) over a sample spacing

 $\eta \Delta x$ (with integer η) rather than Δx ,

$$\frac{D_{(\eta)}^{\alpha}}{D_{(\eta)}x^{\alpha}}h(x) \equiv \frac{1}{(\eta \Delta x)^{\alpha}} \sum_{l=-\infty}^{\infty} c_{l}^{(\alpha)}h(x_{k+\eta l}). \tag{12}$$

We will call the factor η the *scale factor*. The corresponding derivative is measured at the *distance scale* $\ell = \alpha \eta \Delta x$.

Fig. 1 a illustrates this concept. For a simple right-differences scheme as given by Eq. (4), the scale-dependent first derivative is simply the slope of the two points at distance ℓ . For the second derivative given by Eq. (6), we fit a quadratic function through three points with overall spacing ℓ and the curvature of this function is the scale-dependent second derivative.

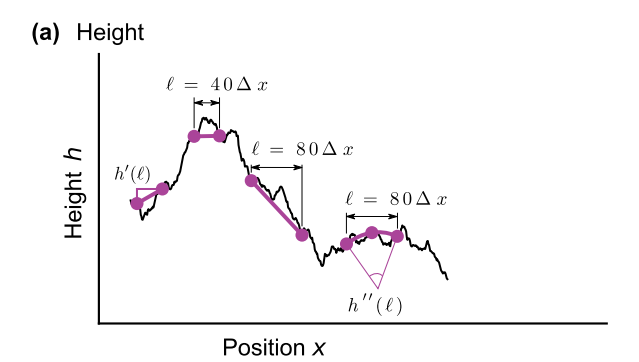
We now define the scale-dependent roughness parameter (SDRP) as

$$h_{\rm SDRP}^{(a)}(\alpha\eta\Delta x) = \left\langle \left(\frac{D_{(\eta)}^{\alpha}}{D_{(\eta)}x^{\alpha}}h(x)\right)^{2}\right\rangle_{\rm domain}^{1/2}.$$
 (13)

This new function defines a series of descriptors for the surface that are analogous to the traditional rms slope $(h_{\rm SDRP}^{(1)} \equiv h_{\rm SDRP}')$ and to the rms curvature $(h_{\rm SDRP}^{(2)} \equiv h_{\rm SDRP}'')$; but instead of being a single scalar value, each represents a curve as a function of the distance scale $\ell = \alpha \eta \Delta x$.

The distance scale ℓ is only clearly defined for the stencils of lowest truncation order. For the n-th derivative, those can be interpreted as fitting a polynomial of order n to n+1 data points (see Fig. 1a). The n-th derivative of this polynomial is then a constant over the width of the stencil; this width must then equal the distance scale ℓ . Higher truncation orders can be interpreted as fitting a polynomial of order m>n to m+1 data points. The n-th derivative is not constant over the stencil and it is not clear what the corresponding length scale is. We will here only use stencils of lowest truncation order where the distance scale is clear.

For non-periodic topographies we need to take care to only include



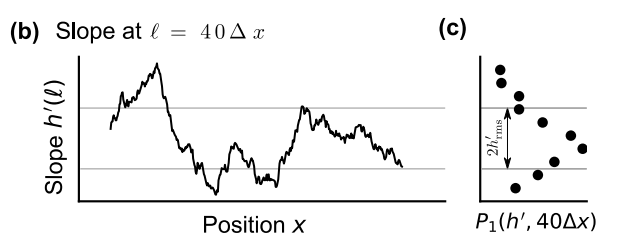


Fig. 1. Illustration of the basic idea behind the scale-dependent roughness parameters. **(a)** Example line scan showing the computation of slopes $h'(\ell)$ and curvatures $h''(\ell)$ from finite differences. A scale can be attached to this computation by computing these finite differences at different distances ℓ , shown for $\ell=40\Delta x$ and $\ell=80\Delta x$ where Δx is the sample spacing. Similarly, the curvature at a finite scale ℓ is given by fitting a quadratic function through three points spaced at a distance $\ell/2$. **(b)** Local slope, obtained at a distance scale of $\ell=40\Delta x$ for the line scan shown in panel (a). The slope is defined for each sample point since we can compute it for overlapping intervals. **(c)** Distribution of the local slope obtained from the slope profile shown in panel (b). The rms slope for this length scale is the width of this distribution.

derivatives that we can actually compute, i.e. where the stencil remains in the domain of the topography. This is indicated by the subscript "domain" in Eq. (13).

2.3. Beyond root-mean-square parameters: Computing the full distribution

The rms value, such as the one defined in Eq. (13), characterizes the amplitude of fluctuations, or the width of the underlying distribution function. Rather than looking at this single parameter, we can also determine the full scale-dependent distribution. Formally we can write this distribution as

$$P_{\alpha}(\chi;\eta) = \left\langle \delta\left(\chi - \frac{D_{(\eta)}^{\alpha}}{D_{(\eta)}\chi^{\alpha}}h(\chi)\right)\right\rangle \tag{14}$$

where $\delta(x)$ is the Dirac- δ function and χ the value of the derivative (of order α) that we are interested in. In any practical (numerical) determination of the distribution, we broaden the δ -function into individual bins and count the number of occurrences of a certain derivative value.

To illustrate this concept on the example of the slope ($\alpha=1$), Fig. 1b shows the scale-dependent derivative at $\ell=40\Delta x$ of the line scan shown in Fig. 1a. The distribution function of the slopes at this scale, $P_1(h', 40\Delta x)$, is then obtained by counting the occurrence of a certain slope value. The resulting distribution is shown in Fig. 1c.

The rms parameters defined in the previous section are the square roots of the second moments of this distribution,

$$h_{\text{SDRP}}^{(a)}(\alpha\eta\Delta x) = \left[\int d\chi \chi^2 P_\alpha(\chi;\eta)\right]^{1/2}.$$
 (15)

The second moment characterizes the underlying distribution fully only if this distribution is Gaussian. We will see below that, for example, scanning probe artifacts introduce deviations from Gaussianity that we can easily detect once we have the full distribution function.

In summary, these probability distributions of arbitrary derivatives (such as slope, curvature, or higher-order functions) serve as an additional set of descriptors for a surface. The distributions are themselves scale dependent, but can be used to compute a wide variety of scale-dependent statistical parameters, including higher cumulants, such as skewness or kurtosis.

3. Analysis: Relationship of scale-dependent roughness parameters to other methods

3.1. Relationship to the autocorrelation function

A common way of analyzing the statistical properties of surface topography is the *height-difference* autocorrelation function, which will be designated here as ACF or $A(\ell)$. (See Ref. [28] for an authoritative discussion of properties and use.) The ACF is defined as

$$A(\ell) = \frac{1}{2} \langle [h(x+\ell) - h(x)]^2 \rangle$$

$$= \left\langle \frac{1}{2} h^2(x) + \frac{1}{2} h^2(x+\ell) - h(x)h(x+\ell) \right\rangle.$$
(16)

Note that some authors call $2A(\ell)$ the *structure function* and use the term ACF for the bare height autocorrelation function $\langle h(x)h(x+\ell)\rangle$ [29,30]. The height ACF and the height-difference ACF are related by

$$A(\ell) = h_{\text{rms}}^2 - \langle h(x)h(x+\ell) \rangle. \tag{17}$$

The ACF has the limiting properties A(0)=0 and $A(\ell\to\infty)=h_{rms}^2$. Equation (16) resembles the finite-differences expression for the first derivative, Eq. (4). Indeed, we can rewrite the ACF as

$$A(\eta \Delta x) = \frac{1}{2} \left\langle \left[\frac{D_{(\eta)}}{D_{(\eta)} x} h(x) \right]^2 \right\rangle (\eta \Delta x)^2$$
 (18)

using the scale-dependent derivative. The scale-dependent rms slope then becomes

$$h'_{\text{SDRP}}(\ell) = [2A(\ell)]^{1/2}/\ell.$$
 (19)

The height-difference ACF can hence be used to compute the scaledependent slope introduced above.

We now show that we can also express higher-order derivatives in terms of the ACF. Using the stencil of the second derivative given in Eq. (6), the scale-dependent second derivative can be written as

$$h_{\text{SDRP}}''(\ell) = \frac{4}{\ell^2} \left\langle \left[h(x + \ell/2) - 2h(x) + h(x - \ell/2) \right]^2 \right\rangle^{1/2}.$$
 (20)

We can rewrite this expression as

$$h_{\text{SDRP}}''(\ell) = \frac{4}{\ell^2} \langle 6h^2(x) - 8h(x)h(x + \ell/2) + 2h(x)h(x + \ell) \rangle^{1/2}.$$
 (21)

and use Eq. (17) to introduce the ACF into this expression, yielding

$$h_{\text{SDRP}}''(\ell) = 4[8A(\ell/2) - 2A(\ell)]^{1/2} / \ell^2.$$
 (22)

Similarly, the scale-dependent third derivative from the stencil given in Eq. (7) becomes

$$h_{\text{SDRP}}^{"}(\ell) = \frac{27}{\ell^3} [30A(\ell/3) - 12A(2\ell/3) + 2A(\ell)]^{1/2}.$$
 (23)

We can therefore relate the scale-dependent root-mean-square slope, curvature, or any other higher-order derivative to the ACF.

In summary, we have shown that the commonly used ACF function can be thought of a specific case of the SDRP analysis: being equivalent to the finite-differences calculation of scale-dependent slope. We further showed that the ACF function can be used as one method to compute higher-order SDRPs.

3.2. Relationship to the variable-bandwidth method

We now introduce an alternative way to arrive at SDRPs based on a different notion of scale. Notice that the discussion leading up to Eq. (13) does not involve the length L of the line scan. This length is only relevant when it comes to determining an upper limit for the stencil length $\ell = \alpha \eta \Delta x$, which is the notion of scale in a measurement based on Eq. (13). Alternatively, we could interpret L as the relevant scale, and study scale-dependent roughness by varying L. This interpretation leads to a class of methods which have been referred to as scaled windowed variance methods [31] or variable bandwidth methods (VBMs). Members of this class of methods differ only in the way that the data is detrended and have been given a variety of names including: bridge method (attributed to Mandelbrot); roughness around the mean height (MHR) [32] (sometimes termed VBM [33]); detrended fluctuation analysis (DFA) [34,35]; and roughness around the rms straight line (SLR) [32].

In all cases, one performs multiple roughness measurements on the same specimen (or the same material) but with different scan sizes L. Plotting the rms height $h_{\rm rms}$ from these measurements versus scan size L, or the rms slope $h'_{\rm rms}$ versus scan resolution (the smallest measurable scale) yields insights into the multi-scale nature of surface topography. An example of an experimental realization of this idea is the classic paper by Sayles & Thomas [36]. The present authors have used and discussed this approach in the past to characterize the topography of diamond thin films [2,3].

These methods can be generalized for the analysis of single measurements. Consider a line scan $h(x_k)$ of length L. The scan is partitioned into $\zeta \geq 1$ segments of length $\ell(\zeta) = L/\zeta$ (with $\ell \leq L$ now being the relevant scale). The dimensionless number ζ , which we call the *magnification*, defines the scale. Some authors use sliding windows rather than exclusive segments [13,32].

The VBM considers the rms height fluctuations in each of the segments, i.e. one computes the standard deviation of the height $h_{\mathrm{VBM},i}(\zeta)$ within segment i at magnification ζ , and then takes the average over all i to compute a scale-dependent $h_{\mathrm{VBM}}(\zeta)$. Some authors (including our own prior work [14]) have tilt corrected the individual segments, i.e. each segment is detrended by subtracting the corresponding mean height and slope (obtained by linear regression of the data in the segment) before computing $h_{\mathrm{VBM},i}(\zeta)$; this approach is called the DFA [34,35] while without tilt correction it is called MHR. In the bridge method, the connecting line between the first and last point in each segment is used for detrending (see e.g. Ref. [33]).

These VBMs are extremely similar to the SDRP. When computing the slope in the SDRP, we compute it by simply connecting the two boundary points at $x=i\ell(\zeta)$ and $x=(i+1)\ell(\zeta)$ with a straight line, as is done in the bridge method. This is distinct from DFA, which uses all data points between the two boundary points and fits a straight line using linear regression. Detrending can be generalized to higher-order polynomials, but this has not been reported in the literature. The relationship between SDRP and VBMs with detrending of order 1 and 2 is conceptually illustrated in Fig. 2.

In DFA, the trend line is simply used as a reference for the computation of fluctuations around it. The coefficients of the detrending polynomial can also be used to analyse how the slope and curvature of the surface depend on scale [37,38]. This yields an alternative measure of the scale-dependent rms slope, $h'_{\mathrm{VBM}}(\zeta)$, obtained at magnification ζ or distance scale $\ell = L/\zeta$. $h'_{\mathrm{VBM}}(\zeta)$ is simply the standard deviation of slopes obtained within all segments i at a certain magnification ζ . We show in the examples below that this scale-dependent slope is virtually identical to the slope obtained from the SDRP.

We can use this idea to extend the DFA to higher-order derivatives. Rather that fitting a linear polynomial in each segment, we detrend using a higher-order polynomial. For extracting a scale-dependent rms curvature, we fit a second-order polynomial to the segment and interpret twice the coefficient of the quadratic term as the curvature. The standard deviation of this curvature over the segments then gives the scale-dependent second derivative, $h''_{VBM}(\zeta)$. Fig. 2 illustrates this concept, again in comparison to the SDRP that for the second-order derivative fits a quadratic function through just three collocation points.

An alternative route of thinking about VBMs is that they use a stencil whose number of coefficients equals the segment length. The stencil can be explicitly constructed from least squares regression (at each scale) of

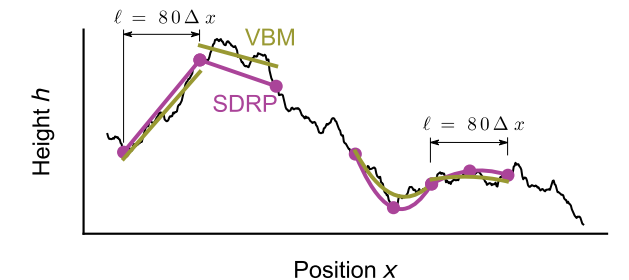


Fig. 2. Illustration of the computation of scale-dependent roughness parameters from the variable bandwidth method (VBM). While in finite differences, the slope is computed between two points at distance ℓ , in the VBM we fit a trend line to a segment of width ℓ . Similarly for the second derivative, the finite-differences estimation fits a quadratic function through three points while in the VBM we fit a quadratic trend line through all data points in an interval of length ℓ .

the polynomial coefficients. The closest equivalent to the SDRP would then be the respective VBM that uses sliding (rather than exclusive) segments. However, even in this case, a remaining difference is that SDRP uses stencils of identical number of coefficients at each scale. In the examples provided in Section 4, we use a VBM that uses nonoverlapping segments.

In summary, we have shown that the various methods for computing scale-dependent height (such as VBM, DFA, and others) can be thought of as a special case of SDRP analysis: where the scale-dependent detrending only occurs for at most linear trend lines. We have then shown how those analyses can be extended to define yet another method for computing SDRPs.

3.3. Relationship to the power spectral density

Finally we outline a fourth way to arrive at SDRPs using the power spectral density (PSD), another common tool for the statistical analysis of topographies [1]. Underlying the PSD is a Fourier spectral analysis, which approximates the topography map as the series expansion

$$h(x) = \sum_{n} a_n \phi_n(x), \tag{24}$$

where $\phi_n(x)$ are called *basis functions*. The Fourier basis is given by

$$\phi_n(x) = \exp(iq_n x),\tag{25}$$

with $q_n = 2\pi n/L$ where L is the lateral length of the sample. The inverse of Eq. (24) gives the expansion coefficients a_n which are typically computed using a fast Fourier-transform algorithm. The PSD is then obtained as [1]

$$C^{1D}(q_n) = L|a_n|^2.$$
 (26)

Fourier spectral analysis is useful because a notion of scale is embedded in the definition Eq. (25): The wavevectors q_n describe plane waves with wavelength $\lambda_n = 2\pi/q_n$.

This basis leads to spectral analysis of surface topography and derivatives are straightforwardly computed from the derivatives of the basis functions,

$$\frac{\partial}{\partial x}\phi_n(x) = iq_n\phi_n(x)$$
 and (27)

$$\frac{\partial^2}{\partial^2 x} \phi_n(x) = -q_n^2 \phi_n(x). \tag{28}$$

We can write the Fourier-derivative generally as

$$\frac{\partial^{\alpha}}{\partial x^{\alpha}}\phi_{n}(x) = \mathscr{D}_{\alpha}(q_{n})\phi_{n}(x) \tag{29}$$

with $\mathscr{D}_1(q_n)=iq_n$ for the first derivative and $\mathscr{D}_2(q_n)=-q_n^2$ for the second derivative. The $\mathscr{D}_a(q_n)$ are complex numbers that we will call the *derivative coefficients*.

The rms amplitude of fluctuations can be obtained in the Fourier picture from Parseval's theorem, that turns the real-space average in Eq. (5) into a sum over wavevectors,

$$h_{\text{rms}}^{(a)} = \left[\sum_{n} |\mathscr{D}_{a}(q_{n})a_{n}|^{2} \right]^{1/2}.$$
 (30)

The notion of a scale-dependence can be introduced in the Fourier picture by removing the contribution of all wavevectors $|q_n| > q_c$ larger than some characteristic wavevector q_c , i.e. setting the corresponding expansion coefficients a_n to zero. This means there are no longer short wavelength contributions to the topography. We will refer to this process as *Fourier filtering*. Fourier filtering can be used to introduce a scale-dependent roughness parameter, e.g.

$$h_{\text{PSD}}^{(a)}(q_c) = \left[\sum_{n} \left| \mathscr{D}_{\alpha}^{\text{F}}(q_n; q_c) \right|^2 C^{\text{1D}}(q_n) \right]^{1/2}$$
 (31)

with $\mathscr{D}_{\alpha}^{F}(q_n;q_c)=\Theta(q_c-|q_n|)\mathscr{D}_{\alpha}(q_n)$ that we call the Fourier-filtered derivative and $\Theta(x)$ is the Heaviside step function. Note that we have expressed Eq. (31) in terms of the PSD, which is typically obtained using a windowed topography if the underlying data is nonperiodic. In the examples that we show in Section 4, we applied a Hann window before computing the scale-dependent derivatives from the PSD.

We now show that Fourier-filtering and finite-differences are related concepts. We first interpret the finite-differences scheme in terms of a Fourier analysis. We apply the finite differences operation to the Fourier basis Eq. (25). This yields

$$\frac{D_{(\eta)}^{\alpha}}{D_{(\eta)}x^{\alpha}}\phi_{n}(x_{k}) = \mathscr{D}_{\alpha}^{s}(q_{n};\eta)\phi_{n}(x_{k})$$
(32)

with

$$\mathscr{D}_{a}^{s}(q_{n};\eta) = \frac{1}{(\eta \Delta x)^{a}} \sum_{l=0}^{\infty} c_{l}^{(a)} \exp(iq_{n}\eta l \Delta x). \tag{33}$$

Note that the right hand side of Eq. (32) is fully algebraic, i.e. it no longer contains derivative operators, and the $\mathscr{D}_a^s(q_n;\eta)$ are (complex) numbers. Inserting these derivative coefficients into Eq. (31) yields Eq. (13). We have therefore unified the description of (scale-dependent) derivatives in the Fourier basis and finite-differences in terms of the derivative coefficients \mathscr{D}_a .

The remaining question is how the scale ℓ used to compute the finite-differences relates to the wavevector q_c used in Fourier-filtering. Fig. 3 shows $\mathscr{D}_1^F(\lambda_c)$ and $D_1^s(\ell)$ for different values of ℓ and λ_c . The location of the maximum of these derivative coefficients agrees if $\eta \Delta x \equiv \ell/\alpha = \lambda_c/2 = \pi/q_c$. For first derivatives ($\alpha=1$), $\ell=\Delta x$. This is the Nyquist sampling theorem, which states that the shortest wavelength we can resolve is $\lambda_c=2\Delta x$. This means to compare SDRP, VBM and PSD, we need to choose a filter cutoff of $q_c=\alpha\pi/\ell$ in the latter. Note that in the SDRP, the (soft) cutoff emerges implicitly from the finite-difference formulation.

In summary, we have shown that the SDRPs, which were defined in real-space in Section 2.2, can be equivalently computed in frequency-space using the PSD. The results should be the same, however, frequency-space calculations have the shortcomings that nonperiodic topographies need to be windowed, and a filter cutoff needs to be applied.

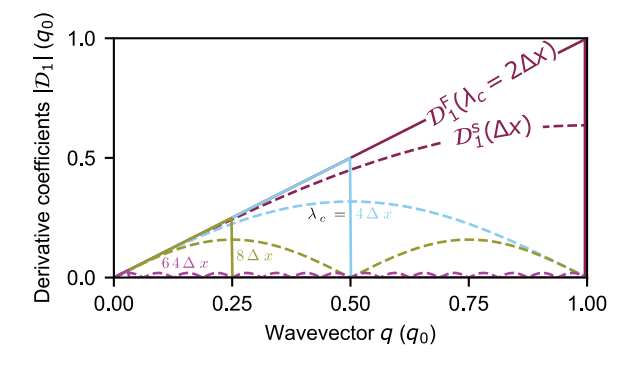


Fig. 3. Derivative coefficients for finite differences \mathscr{D}_1^s and the Fourier-filtered derivative \mathscr{D}_1^F for different distance scales ℓ . The coefficients agree at small wavevectors q. The maximum of the coefficient agrees if the filter wavelength $\lambda_c = 2\ell$, corresponding to the Nyquist sampling theorem (see text).

3.4. Summary notes about comparison to other methods

In this section, we have shown that three of the most common methods for roughness characterization, namely ACF, VBM, and PSD, are highly related to the SDRP. In fact, some form of SDRP can be computed using any of these three methods, instead of using the original definition, Eq. (13), with approximately equivalent results (see numerical experiments in the next section). Intuitively, the SDRP can be thought of as a general framework for analysis, which contains ACF, VBMs and PSD as special cases.

4. Discussion: Application of scale-dependent roughness parameters, and advantages over other methods

4.1. Application to a synthetic self-affine surface

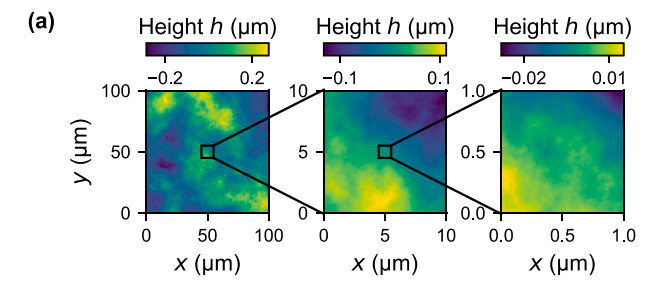
We first apply the concepts presented above to a synthetic self-affine topography. The topography has been first presented in Ref. [1] and consists of three virtual "measurements" of a large (65 536 \times 65 536 pixels) self-affine topography generated with a Fourier-filtering algorithm [1,39]. This algorithm works as follows: We superpose sine waves with uncorrelated random phases and amplitudes scaled according to a power-law. On the pixel at position $\vec{x}_{ij} = (x_i, y_j)$, the height can be written as

$$h_{ij} = \sum_{\substack{l \neq l \geq 0 \\ |\overrightarrow{q}_{kl}| < q_s}} A_{kl} \sin\left(\overrightarrow{q}_{kl} \cdot \overrightarrow{x}_{ij} + \phi_{kl}\right), \tag{34}$$

where $\overrightarrow{q}_{kl}=2\pi/L(k,l)$ is the wavevector and L is the period of the topography. The phases ϕ_{kl} are uncorrelated and uniformly distributed between 0 and 2π . The amplitudes A_{kl} are uncorrelated Gaussian random variables with variance proportional to $|\overrightarrow{q}_{kl}|^{-2-2H}$. The sum runs only over wavevectors smaller than the short-wavelength cutoff $q_s=2\pi/\lambda_s$. The (two-dimensional) PSD of the surface is the square of the amplitudes A_{kl} and is 0 for wavelengths below λ_s . We generated the surface with Hurst exponent H=0.8, cutoff wavelength $\lambda_s=10$ nm, pixel size $\Delta x=\Delta y=2$ nm and physical size L=131 µm. This surface was subsampled in three blocks of 500×500 pixels at overall lateral sizes of $100~\mu m\times100~\mu m$, $10~\mu m\times10~\mu m$ and $1~\mu m\times1~\mu m$ to emulate measurement at different resolution. Each of these virtual measurements is nonperiodic and independently tilt-corrected. The data for the three subsampled topographies is available online [40].

Fig. 4a shows the topography map of these three emulated measurements. The measurements zoom subsequently into the center of the topography. The one-dimensional PSDs ($C^{\rm 1D}$, Fig. 4b) of the three topographies align well, showing zero power below the cutoff wavelength of $\lambda_{\rm 5}$. Note that unlike most authors (with few exceptions in geophysics [41–45]) or even our own prior work, we display the PSD as a function of wavelength $\lambda=2\pi/q$ where q is the wavevector; this facilitates comparison with the real-space techniques introduced above, and also wavelengths are more intuitively understandable than wavevectors. Since the topography is self-affine, the PSD scales as $C^{\rm 1D} \propto \lambda^{1+2H}$ as indicated by the solid line.

The ACF (or rather its square root) is shown in Fig. 4c. The ACF and all other scale-dependent quantities reported below are obtained from averages over adjacent line scans, i.e. from one-dimensional profiles rather than two-dimensional area scans. This is compatible with how C^{1D} is computed (see Ref. [1]). The ACFs from the three measurements line up and follow $\sqrt{A} \propto \ell^H$ (see solid black line in Fig. 4c). Note that the ACF does not drop to zero for $\ell < \ell_s \equiv \lambda_s/2$ as the PSD did. This behavior becomes clearer by inspecting the scale-dependent slope $h_{\rm SDRP}'(\ell) = \sqrt{2A(\ell)}/\ell$ that saturates at a constant value for $\ell < \ell_s$. This is the true rms slope that is computed when all scales are considered. For large ℓ , the rms slope scales as $h_{\rm SDRP}' \propto \ell^{H-1}$ (solid black line in Fig. 4d).



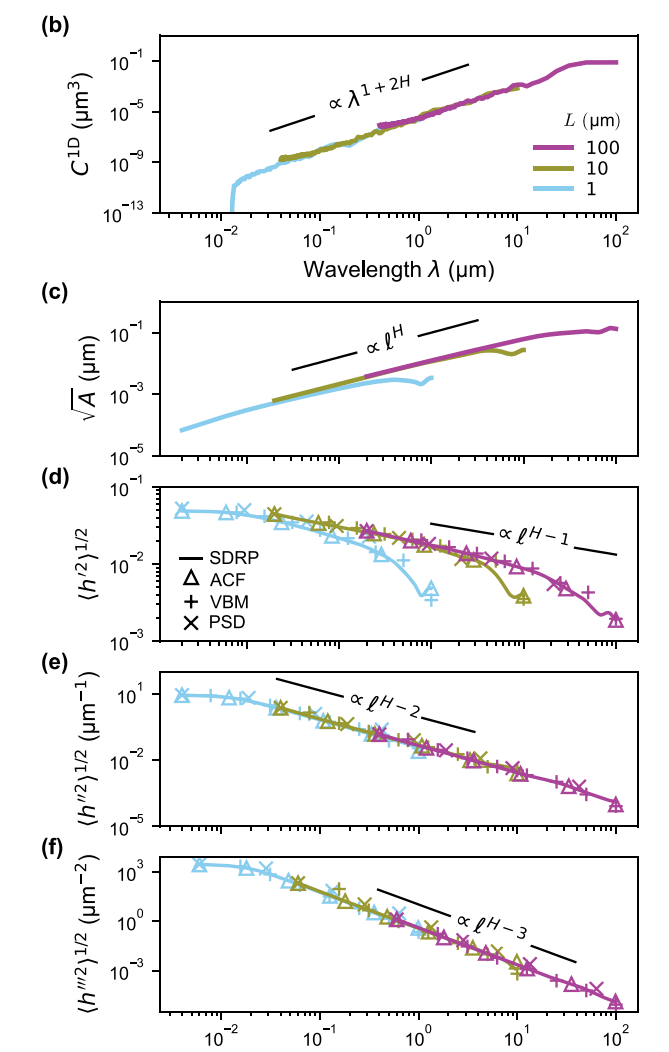


Fig. 4. Example of scale dependent-roughness parameters for an ideal self-affine surface with Hurst exponent H=0.8. (a) A large surface was subsampled in three topographies of 500×500 pixels at different resolution. (b) Individual PSDs displayed as a function of wavelength $\lambda=2\pi/q$, where q is the wavevector. (c) Square root of the ACF displayed as a function of distance scale ℓ . (d) Scale-dependent rms slope. (e) Scale-dependent rms curvature. (f) Third derivative as an example of how this method can be used to go beyond traditional analysis. Color is used to distinguish the three different topographies. The figure shows results from the four SDRPs (finite-differences based SDRP, ACF, VBM and PSD), showing that the results agree. The solid black lines in panels (b-f) shows the power-law scaling of an ideal self-affine topography with Hurst exponent H. Note that the deviations from power-law scaling at large scales are especially visible in panels (c) and (d) because of the smaller range of values on the y-axis.

Distance scale \(\ell \) (µm)

Finally, we display the scale-dependent curvature $h''_{\mathrm{SDRP}}(\ell)$ in Fig. 4e. Like the rms slope, the curvature saturates for $\ell < \ell_s$ to the "true" small-scale value of the curvature. The curvatures of the three individual measurements again line up and follow $h''_{\mathrm{SDRP}}(\ell) \propto \ell^{H-2}$ because of the self-affine character of the overall surface. The rms curvature computed from the ACF (Eq. (22)) is strictly only applicable to periodic topographies, but in our numerical experiments the ACF agrees with the original definition of the SDRPs (Eq. (13)) within the thickness of the line. The errors occur at large distance scales and can, in principle, lead to negative values of h''_{SDRP} , but we have not seen this occurring in the numerical data presented in this paper.

In our derivation above we have presented alternative routes for obtaining scale-dependent roughness parameters from the VBM and PSD. The plusses (+) in Figs. 4d and e show the rms slope and curvature obtained using the VBM, while the crosses (x) show the results obtained using the PSD. They align well with the respective parameters obtained from the SDRP and only deviate at large scales. In summary, all three routes (ACF, VBM, PSD) for obtaining SDRPs are equally valid and lead to results that are consistent with those computed using the original definition (Eq. (13)). The advantage of the SDRP, ACF and the VBM over the PSD is that they are directly (without windowing) applicable to nonperiodic data.

We have now demonstrated four independent ways of obtaining scale-dependent slopes, curvatures and higher-order derivatives. We would like to point out that all four routes constitute novel uses of the underlying analysis methodology. Our primary tool in what follows will be the SDRP; however, we have demonstrated that the ACF, VBM and

PSD yield equivalent results. The broader importance of using scale-dependent slopes and curvatures over the "bare" ACF, VBM or PSD is that it is straightforward to interpret the meaning of these parameters. We all have intuitive understanding of the meaning of slopes and curvatures, whereas it is difficult to ascribe a geometric meaning to a value of the PSD (that can even differ in unit, see discussion in Ref. [1]).

4.2. Detecting tip artifacts in simulated topography measurements

We now turn to another example, the analysis of tip artifacts. This will exploit a power of the SDRP, namely the fact that we can compute the full underlying distribution of arbitrary derivatives outlined in Section 2.3.

Fig. 5a shows two computer generated nonperiodic topographies of size 0.1 μ m \times 0.1 μ m. The first topography is pristine and was generated using the Fourier-filtering algorithm mentioned above. As in the previous example, we ensured the scan is not periodic by taking a section of a larger (0.5 μ m) periodic scan. The second topography contains tip artifacts and was obtained from the pristine surface using the following nonlinear procedure: For every location (x_i, y_i) on the topography we lower a sphere with radius $R_{\rm tip}$ (here 40 nm) towards a position (x_i, y_i, z_i) until the sphere touches the pristine topography anywhere. The resulting z-position z_i of the sphere is then taken as the "measured" height of the topography. This topography was discussed in Ref. [1] and the data files are available at Ref. [46]. The two curves underneath the maps in Fig. 5a are cross-sections through the middle of the respective topography.

It is clear from simply looking at the data in Fig. 5a that the scanning

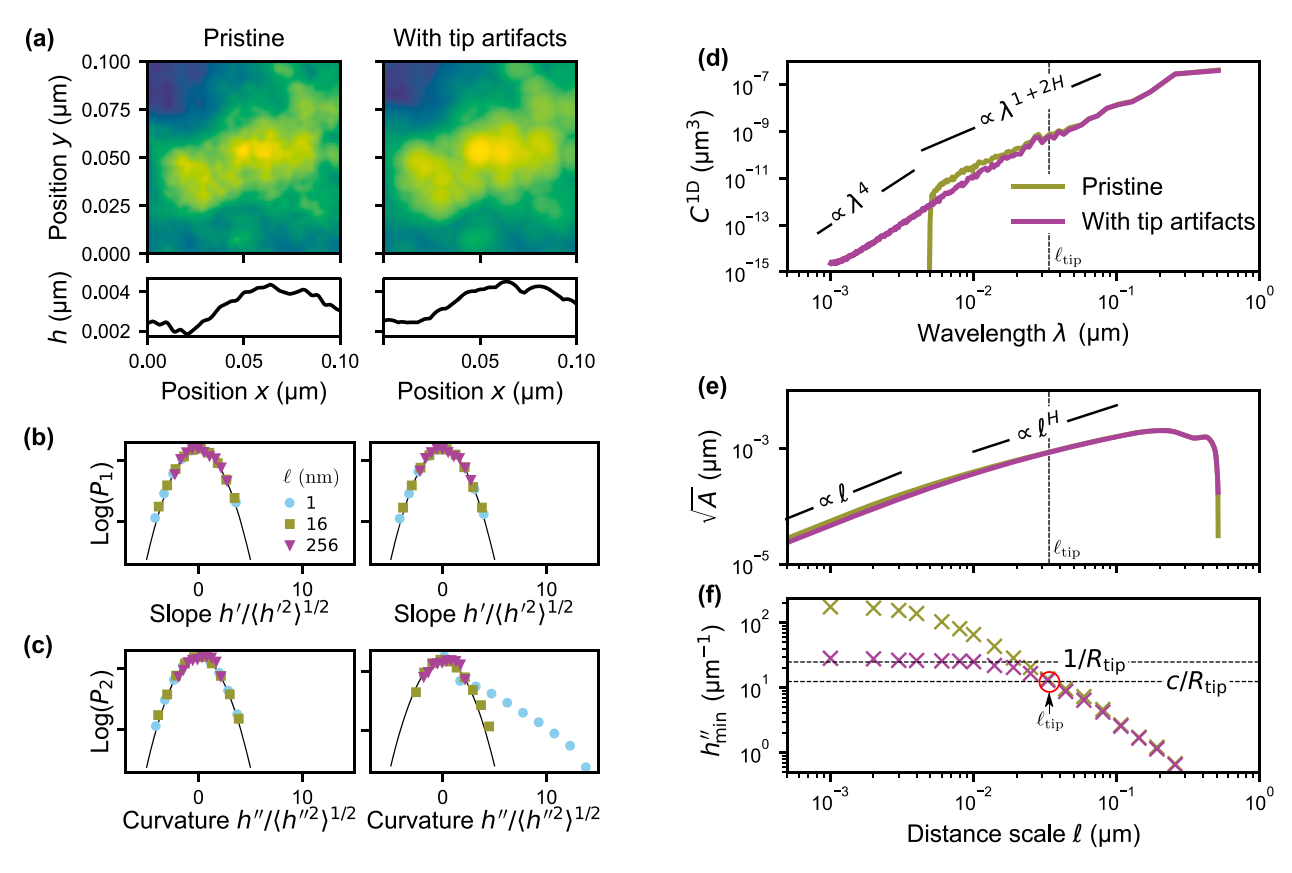


Fig. 5. Scale-dependent roughness parameters for the analysis of tip artifacts. (a) A computer-generated "pristine" topography was scanned with a virtual tip of $R_{\rm tip} = 40$ nm radius. The bottom row shows cross-sectional profiles of the maps shown above. The artifacted map and profile show clear blunting of the peaks and cusps in the valleys (see text for more discussion). (b) Distribution of slopes at distance scales $\ell = 1$ nm (circles •), 16 nm (squares •) and 256 nm (triangles •). (c) Distribution of curvatures at these scales. Both slopes and curvatures are obtained in the x-direction. The left plots in (b) and (c) show the computed values for the pristine surface, while the right plots in these panels show the values for the tip-artifacted measurement. Black solid lines show the normal distribution. (d) PSDs and (e) ACFs of both topographies. (f) The plot of minimum curvature h''_{\min} (see text) shows a clear deviation between the pristine and artifacted measurement that starts at approximately the point where the scale-dependent minimum curvature equals the radius of the tip.

probe smoothens the peaks of the topography. Indeed the curvature near the peaks must be equal to $-1/R_{\rm tip}$. Conversely, the valleys look like cusps that originate from the overlap of two spherical bodies. These cusps are sharp and should lead to large (in theory unbounded, but in practice bounded by resolution and noise) positive values of the curvature. Church & Takacs [47,48] have pointed out that tip artifacts should lead to PSD $C^{\rm 1D}(q) \propto q^{-4}$, which is precisely a result of the cusps in the topography. (The Fourier transform of a triangle scales as q^{-2} , such that the PSD $\propto q^{-4}$.) We have demonstrated in Refs. [1,3] numerically that this is indeed the case.

We are now in a position to more precisely look at the effect of tip radius. Fig. 5b shows the scale-dependent slope distribution $P_1(h^{'},\ell)$, normalized by the rms slope at the respective scale. The black solid line shows a Gaussian distribution (of unit width) for reference. It is clear that both our pristine topography (left columns) and the topography with tip-radius artifacts (right column) follow a Gaussian distribution for the scale dependent slopes across scales from 1 nm to 256 nm shown in the figure.

The situation is different for the scale-dependent curvature, shown in Fig. 5c. While the pristine surface (left column) follows a Gaussian distribution, the topography with tip-radius artifacts is only Gaussian for larger scales ($\ell=16$ nm and 256 nm). There is a clear deviation at the smallest scales, showing an exponential distribution for positive curvature values, corroborrating the empirical discussion above that cusps leads to large positive values for the curvature. As argued above and in Refs. [47,48], these cusps lead to a PSD $\propto q^{-4} \propto \lambda^4$. Fig. 5d shows the PSDs of both topographies. The artifacted surface indeed crosses over to $C^{1D} \propto \lambda^4$ at a wavelength of $\lambda \sim 20-40$ nm.

We note this cross-over to λ^4 is subtle and difficult to detect in measured data. Other measures, such as the ACF shown in Fig. 5e, are unsuitable to detect these artifacts. The region where the $C^{1D} \propto \lambda^4$ shows up as a linear region in the square root of the ACF, $\sqrt{A} \propto \ell$. The exponent of 1 from that region is too close to the exponent of H=0.8 to be clearly distinguishable. The present authors have previously suggested a tipradius reliability cutoff [1,2], where the scale-dependent rms curvature was compared to the tip curvature. Based on similar ideas, we now propose an additional metric that is intended to more accurately detect the onset of the tip-radius artifact.

Rather than computing the width of the distribution as do the rms measures, we now ask the question of what is the *minimum* curvature value found at a specific scale ℓ . We therefore evaluate

$$h_{\min}^{"}(\ell) = -\min_{k} \left[\frac{D_{(\ell)}^2}{D_{(\ell)} x^2} h(x_k) \right].$$
 (35)

The crosses in Fig. 5f show this quantity for the pristine and the artifacted surface. It is clear that at small scales the curvature of the pristine surface is larger than the artifacted one. Additionally, the artifacted surface settles to $h_{\min}''(\ell) \approx 1/R_{\rm tip}$ as $\ell \! - \! 0$. This is a clear indicator that the curvature of the peaks on the artifacted surface is given by the tip radius and that in principle, the tip radius can be deduced from h_{\min}'' . However, in real AFM data, h_{\min}'' has no well defined $\ell \! - \! 0$ limit because there are noise sources not considered in our simulated measurement. The tip radius then needs to be determined from auxiliary measurements (see next section).

For each tip radius and surface topography, there is a critical length scale $\ell_{\rm tip}$ below which AFM data is unreliable. We estimate $\ell_{\rm tip}$ by numerically solving

$$h_{\min}''(\ell_{\rm tip}) = c/R_{\rm tip} \tag{36}$$

for ℓ_{tip} using a bisection algorithm. The empirical factor c needs to be close to or slightly smaller than unity. Fig. 5f shows this condition as a dashed horizontal line. Note that ℓ_{tip} depends both on the tip radius and the curvature of the measured surface: measurements on rough surfaces

have more tip artifacts than measurements on smooth surfaces because a tip that can conform to the valleys of a smooth surface may not be able to sample the valleys on a rougher surface. We also indicate the scale $\ell_{\rm tip}$ in the ACF (Fig. 5e) and in the PSD. The factor c=1/2 was chosen such that $\lambda_{\rm tip}$ marks the crossover from artifacted $C^{\rm 1D} {\propto} \lambda^4$ to the pristine $C^{\rm 1D} {\propto} \lambda^{1+2H}.$ We will use the same factor when analyzing experimental data in the next section, where there is no "pristine" measurement available for comparison.

Our proposed measure is useful because it can be robustly and automatically carried out on large sets of measurements; by contrast, the detection of $C^{\rm 1D} \propto \lambda^4$ is difficult because fitting exponents requires data over at least a decade in length and carries large errors [49].

4.3. Application to an experimental measurement

As a final example, we turn to an experimental analysis of an ultrananocrystalline diamond (UNCD) film that has been described in detail in Ref. [2]. Fig. 6a shows a single representative AFM scan of that surface available online at Ref. [50]. The peaks have rounded tips similar to the synthetic scan shown in Fig. 5a. The curvature distribution (Fig. 6b) also has a similar characteristic to our synthetic topography (Fig. 5c). At large scales, the distribution is approximately Gaussian (shown by the solid black line). At smaller scales, we see deviations to higher curvature

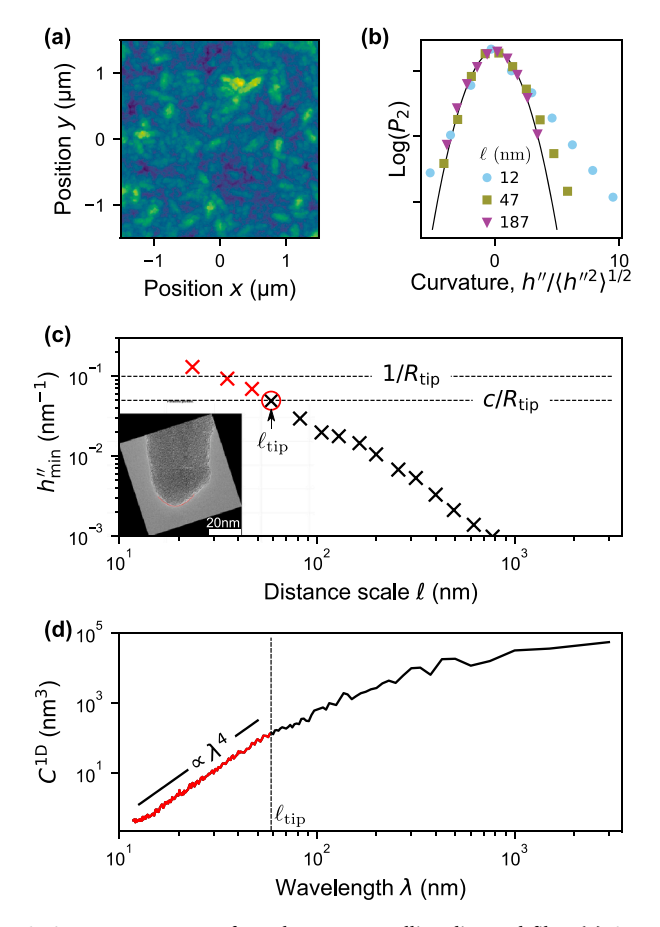


Fig. 6. AFM measurement of an ultrananocrystalline diamond film. (a) AFM measurement showing the smoothing of peaks similar to the emulated scans shown in Fig. 5a. (b) Normalized curvature distribution at distance scales $\ell=12$ nm (circles •), 47 nm (squares •) and 187 nm (triangles •). $\ell=12$ nm corresponds to a scale factor $\eta=1$. (c) We use the peak curvature $h_{\min}^{\prime\prime}$ (see text) to estimate the scale $\ell_{\rm tip}$ below which the AFM data is unreliable (highlighted in red). The empirical constant c=1/2. Inset: TEM image of the AFM tip. Fitting a parabola to the tip yields a radius $R_{\rm tip}$ of 10 nm. (d) Power spectral density (PSD) of the measurement. The black solid line shows scaling with λ^4 that indicates tip artifacts.

values, indicative of the cusps that are characteristic of tip artifacts. We also see a minor deviation to higher negative curvatures, which we attribute to additional instrumental noise that contributes to small-scale features of the data.

These negative curvatures prevent the conclusive determination of the tip radius from the scale-dependent tip curvature (Fig. 6c). Unlike the synthetic surfaces, the scale-dependent tip curvature $h_{\min}''(\ell)$ (Fig. 5f) does not saturate to a specific value at small distances ℓ . Instead, we determined the radius of AFM tip from auxiliary transmission electron microscopy (TEM) measurements (Fig. 6c inset). For the measured $R_{\rm tip}=10$ nm, we can identify the region where $h_{\min}''(\ell)>1/(2R_{\rm tip})$ as unreliable, leading to a lateral length-scale of around $\ell_{\rm tip}\approx 60$ nm below which the data is no longer reliable. The PSD (Fig. 6d) shows λ^4 scaling below the characteristic wavelength $\ell_{\rm tip}$.

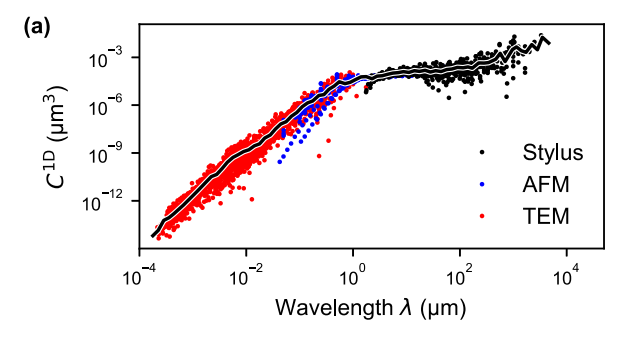
After having looked at tip-radius effects on single measurements, we now turn to applying SDRPs to the full experimental dataset from Ref. [2], where a total of 126 individual measurements from three different instruments, a stylus profilometer, an AFM and a TEM, were combined to extract the power spectrum of the surface over eight orders of magnitude. (The dataset is available online at Ref. [51].) Fig. 7 shows the PSD, ACF, rms slope and rms curvature for each individual measurement as well as an average curve representative of the whole surface. For each tip-based measurement (stylus and AFM), we computed the critical scale $\ell_{\rm tip}$ using Eq. (36) as above and excluded data on scales below $\ell_{\rm tip}$. The good overlap of the AFM data with the TEM data confirms that this procedure removed tip artifacts. The full data set (see Ref. [2]) shows clear regions where the PSD $C^{\rm 1D} \propto q^{-4}$.

As shown in Fig. 7, all four methods can be used to stitch together the data from a large set of measurements to obtain the resulting SDRP of the underlying physical surface. The ACF (Fig. 7b) and rms slope $h'_{\rm rms}$ (Fig. 7c) of the TEM measurements curve down at large ℓ , an effect also seen (but less pronounced) in our synthetic data of Fig. 4c and d. This is a consequence of tilt correction, that enforces zero slope at the size of the overall measurement, hence forcing $h'_{\rm rms}$ to drop towards zero. While more sophisticated schemes for tilt correction could be devised to eliminate this long-wavelength artifact, the rms curvature $h''_{\rm rms}$ is free of this artifact as it is unaffected by local tilt of the measurement. We therefore advocate that it is important to look at a combination of these scale-dependent analysis techniques rather than relying on a single one.

5. Summary & conclusions

First, we demonstrated the calculation of scale-dependent parameters using a finite-differences scheme, with a variable distance scale. We have termed this characterization of first- and higher-order derivatives the scale-dependent roughness parameter (SDRP) analysis. Then we showed that the commonly used height-difference autocorrelation function (ACF) can be interpreted as the scale-dependent root-meansquare (rms) finite-difference slope. This leads to a straightforward generalization of the ACF for higher derivatives, yielding for example a scale-dependent rms curvature. We have further generalized this analysis to compute distributions of roughness parameters as a function of scale; the curvature distribution analysis can be used to identify tipradius artifacts. To connect our analysis to conventional techniques, we have shown how equivalent scale-dependent roughness parameters can be computed not only from the ACF, but also from the the variable bandwidth method and the power spectral density. We demonstrated the successful use of these analyses to describe computer-generated and experimentally measured surfaces. Additional work is ongoing to apply this analysis on a wide range of surfaces, for example surfaces with facets [3] or periodic structures.

In summary, we proposed a novel SDRP analysis, and demonstrated how this is a generalization of commonly used roughness metrics. We suggest that this SDRP approach serves to harmonize competing roughness descriptors, but also offers advantages over those other



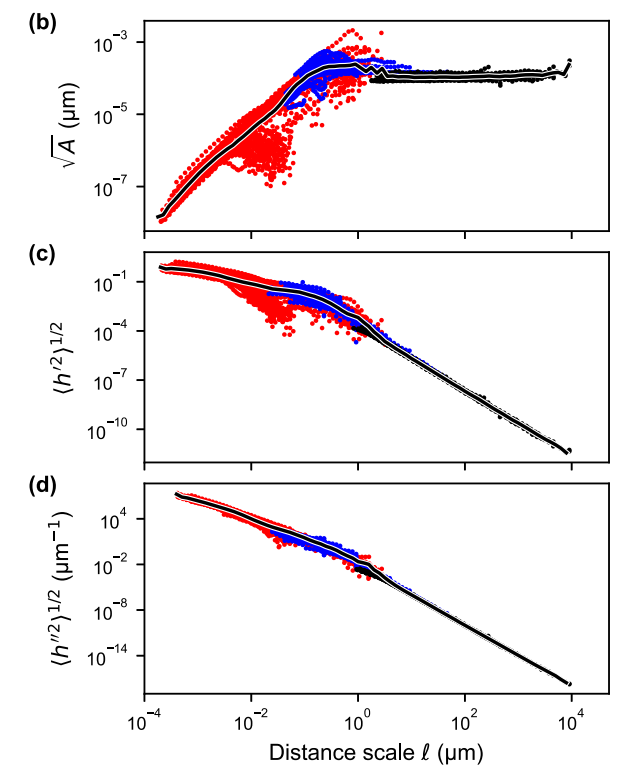


Fig. 7. Topography measurements of an ultrananocrystalline diamond film are combined across eight orders of magnitude of scales using the PSD (a), ACF (b), rms slope (c) and rms curvature (d). For each of these measures, we obtain a curve representative of the surface by averaging over all the individual measurements (solid black line). For tip-based methods, AFM and stylus profilometry, we used the criterion proposed in Section 4.2 to exclude unreliable scales.

methods, especially in terms of ease of calculation, intuitive interpretability, and detection of artifacts.

Data availability statement

All the underlying synthetic and experimental scans are available at https://contact.engineering. Individual datasets are referenced throughout the paper.

Declaration of Competing Interest

The authors declare that they have no known competing financial interests or personal relationships that could have appeared to influence the work reported in this paper.

Acknowledgements

LP thanks the Deutsche Forschungsgemeinschaft (project EXC-2193/ 1 – 390951807) and the European Research Council (StG-757343) for

Science Foundation under award number CMMI-1727378.

Appendix A. Generalization to two dimensions

We here briefly outline the generalization of the SDRP to two-dimensions. The main difference is that in two dimensions the derivative becomes the (discrete) gradient (Dh/Dx, Dh/Dy), the curvature becomes the Hessian $(D^2h/Dx^2, D^2h/Dy^2, D^2h/DxDy)$ and higher-order derivatives contain additional cross terms. All averages are carried out over areas, not line scans. We can then for example define a scale-dependent gradient as

$$h_{\text{SDRP}}^{',\text{2D}}(\ell) = \left\langle \left(\frac{D_{(\ell/\Delta x)}}{D_{(\ell/\Delta y)}x} h(x,y) \right)^2 + \left(\frac{D_{(\ell/\Delta y)}}{D_{(\ell/\Delta y)}y} h(x,y) \right)^2 \right\rangle^{1/2}, \tag{A.1}$$

where the average $\langle \cdot \rangle$ now runs over the area. We note that in two-dimensions the situation may arise, where the scale factors $\eta_x = \ell / \Delta x$ and $\eta_y = \ell$ $/\Delta y$ are no longer integer; this in particular happens if the aspect ratio of the individual pixel is not unity, $\Delta x \neq \Delta y$. In this case the additional (numerical) complexity arises, that one needs to interpolate between data points to measure the derivatives at the same distance scale in x- and

References

- [1] T.D.B. Jacobs, T. Junge, L. Pastewka, Quantitative characterization of surface topography using spectral analysis, Surf. Topogr. Metrol. Prop. 5 (2017) 013001.
- [2] A. Gujrati, S.R. Khanal, L. Pastewka, T.D.B. Jacobs, Combining TEM, AFM, and profilometry for quantitative topography characterization across all scales, ACS Appl. Mater. Interf. 10 (2018) 29169.
- A. Gujrati, A. Sanner, S.R. Khanal, N. Moldovan, H. Zeng, L. Pastewka, T.D. B. Jacobs, Comprehensive topography characterization of polycrystalline diamond coatings, Surf. Topogr. Metrol. Prop. 9 (2021) 014003.
- 4287 ISO, Geometrical product specifications (GPS)-Surface texture: Profile method, Standard, Geneva: International Organization for Standardization, 1997.
- B. Mandelbrot, How long is the coast of Britain? Statistical self-similarity and fractional dimension, Science 156 (1967) 636.
- [6] B.B. Mandelbrot, The fractal geometry of nature, W. H. Freeman, 1982.
- S. Dalvi, A. Gujrati, S.R. Khanal, L. Pastewka, A. Dhinojwala, T.D.B. Jacobs, Linking energy loss in soft adhesion to surface roughness, Proc. Natl. Acad. Sci. USA 116 (2019) 25484.
- [8] B.B. Mandelbrot, D.E. Passoja, A.J. Paullay, Fractal character of fracture surfaces of metals, Nature 308 (1984) 721.
- [9] L. Ponson, D. Bonamy, E. Bouchaud, Two-dimensional scaling properties of experimental fracture surfaces, Phys. Rev. Lett. 96 (2006) 035506.
- [10] D. Bonamy, L. Ponson, S. Prades, E. Bouchaud, C. Guillot, Scaling exponents for fracture surfaces in homogeneous glass and glassy ceramics. Phys. Rev. Lett. 97 (2006) 135504.
- [11] E. Nadgorny, J. Schwerdtfeger, F. Madani-Grasset, V. Koutsos, E.C. Aifantis, M. Zaiser, Evolution of self-affine surface roughness in plastically deforming KCl single crystals. Proceedings of International conference on Statistical Mechanics of Plasticity and Related Instabilities - PoS(SMPRI2005) volume 023, 2006, p. 012.
- [12] J. Schwerdtfeger, E. Nadgorny, F. Madani-Grasset, V. Koutsos, J.R. Blackford, M. Zaiser, Scale-free statistics of plasticity-induced surface steps on KCl single crystals, J. Stat. Mech. – Theory Exp. 2007 (2007) L04001.
- S. Sandfeld, M. Zaiser, Deformation patterns and surface morphology in a minimal model of amorphous plasticity. J. Stat. Mech. - Theory Exp. 2014 (2014) P03014.
- [14] A.R. Hinkle, W.G. Nöhring, R. Leute, T. Junge, L. Pastewka, The emergence of small-scale self-affine surface roughness from deformation, Sci. Adv. 6 (2020). Faax0847.
- [15] B.N.J. Persson, On the fractal dimension of rough surfaces, Tribol. Lett. 54 (2014)
- [16] A.W. Bush, R.D. Gibson, T.R. Thomas, The elastic contact of a rough surface, Wear 35 (1975) 87.
- [17] B.N.J. Persson, Elastoplastic contact between randomly rough surfaces, Phys. Rev. Lett. 87 (2001) 116101.
- [18] B.N.J. Persson, Theory of rubber friction and contact mechanics, J. Chem. Phys. 115 (2001) 3840.
- [19] B.N.J. Persson, E. Tosatti, The effect of surface roughness on the adhesion of elastic solids, J. Chem. Phys. 115 (2001) 5597.
- [20] B.N.J. Persson, Adhesion between elastic bodies with randomly rough surfaces, Phys. Rev. Lett. 89 (2002) 245502.
- [21] S. Hyun, L. Pei, J.-F. Molinari, M.O. Robbins, Finite-element analysis of contact etween elastic self-affine surfaces, Phys. Rev. E 70 (2004) 026117.
- [22] C. Campañá, M.H. Müser, Contact mechanics of real vs. randomly rough surfaces: a Green's function molecular dynamics study, EPL 77 (2007) 38005. M.H. Müser, Rigorous field-theoretical approach to the contact mechanics of rough
- elastic solids, Phys. Rev. Lett. 100 (2008) 055504. L. Pastewka, M.O. Robbins, Contact between rough surfaces and a criterion for
- macroscopic adhesion, Proc. Natl. Acad. Sci. USA 111 (2014) 3298.
- [25] M.S. Longuet-Higgins, The statistical analysis of a random, moving surface, Philos. Trans. R. Soc. Lond. A 249 (1957) 321.

- [26] M.S. Longuet-Higgins, Statistical properties of an isotropic random surface, Philos. Trans. R. Soc. Lond. A 250 (1957) 157.
- P.R. Nayak, Random process model of rough surfaces, J. Lubr. Technol. 93 (1971) 398.
- **[28]** A. Wang, M.H. Müser, On the usefulness of the height-difference-autocorrelation function for contact mechanics, Tribol. Int. 123 (2018) 224.
- [29] R.S. Sayles, T.R. Thomas, The spatial representation of surface roughness by means of the structure function: a practical alternative to correlation, Wear 42 (1977) 263.
- [30] T.R. Thomas, Rough surfaces, World Scientific, 1998.
- [31] M.J. Cannon, D.B. Percival, D.C. Caccia, G.M. Raymond, J.B. Bassingthwaighte, Evaluating scaled windowed variance methods for estimating the hurst coefficient of time series, Physica A 241 (1997) 606.
- G. Moreira, J.d. Silva, S. Kamphorst, On the fractal dimension of self-affine profiles, J. Phys. A 27 (1994) 80794089.
- [33] J. Schmittbuhl, J.-P. Vilotte, S. Roux, Reliability of self-affine measurements, Phys. Rev. E 51 (1995) 131.
- C.-K. Peng, S.V. Buldyrev, S. Havlin, M. Simons, H.E. Stanley, A.L. Goldberger, Mosaic organization of DNA nucleotides, Phys. Rev. E 49 (1994) 1685.
- [35] C.K. Peng, S. Havlin, H.E. Stanley, A.L. Goldberger, Quantification of scaling exponents and crossover phenomena in nonstationary heartbeat time series, Chaos 5 (1995) 82.
- [36] R.S. Sayles, T.R. Thomas, Surface topography as a nonstationary random process, Nature 271 (1978) 431.
- [37] P. Podsiadlo, M. Wolski, G.W. Stachowiak, Novel directional blanket covering method for surface curvature analysis at different scales and directions, Tribol Lett 65 (2017) 2.
- [38] P. Podsiadlo, M. Wolski, G.W. Stachowiak, Directional signatures of surface texture, Tribol Lett 67 (2019) 109.
- S.B. Ramisetti, C. Campañá, G. Anciaux, J.-F. Molinari, M.H. Müser, M.O. Robbins, The autocorrelation function for island areas on self-affine surfaces, J. Phys. Condens. Matter 23 (2011) 215004.
- [40] T.D.B. Jacobs, T. Junge, L. Pastewka, Self-affine synthetic surface, 2020. https:// contact.engineering/go/867nv/.
- A. Sagy, E.E. Brodsky, G.J. Axen, Evolution of fault-surface roughness with slip, Geology 35 (2007) 283
- [42] T. Candela, F. Renard, Y. Klinger, K. Mair, J. Schmittbuhl, E.E. Brodsky, Roughness of fault surfaces over nine decades of length scales, J. Geophys. Res. - Sol. Ea. 117 (2012).B08409.
- [43] E.E. Brodsky, J.D. Kirkpatrick, T. Candela, Constraints from fault roughness on the scale-dependent strength of rocks, Geology 44 (2016) 19.
- T. Candela, E.E. Brodsky, The minimum scale of grooving on faults, Geology 44
- [45] C.A. Thom, E.E. Brodsky, R.W. Carpick, G.M. Pharr, W.C. Oliver, D.L. Goldsby, Nanoscale roughness of natural fault surfaces controlled by scale-dependent yield strength, Geophys. Res. Lett. 44 (2017) 9299.
- [46] T.D.B. Jacobs, T. Junge, L. Pastewka, Synthetic self-affine topography scanned with a virtual spherical probe, 2021. https://contact.engineering/go/v9qwe/.
- [47] E.L. Church, P.Z. Takacs, Instrumental Effects in Surface Finish Measurement. Proc. SPIE 1009, Surface Measurement and Characterization, 1989, pp. 46-55.
- [48] E.L. Church, P.Z. Takacs, Effects of the Nonvanishing Tip Size in Mechanical Profile Measurements. Proc. SPIE 1332, Optical Testing and Metrology III: Recent Advances in Industrial Optical Inspection, 1991, pp. 504-514.
- A. Clauset, C. Shalizi, M. Newman, Power-law distributions in empirical data, SIAM Rev. 51 (2009) 661.
- [50] A. Sanner, L.A. Thimons, W.G. Nöhring, T.D.B. Jacobs, L. Pastewka, Unpolished UNCD (measured with 10.11 nm AFM tip), 2021. https://contact.engineering/go/ mvttv/.
- A. Gujrati, S.R. Khanal, L. Pastewka, T.D.B. Jacobs, Ultrananocrystalline diamond (UNCD) (2020) https://contact.engineering/go/8sc7t/.